7

Study of Thin Oxide Films with NC-AFM: Atomically Resolved Imaging and Beyond

M. Heyde, G.H. Simon, and T. König

Abstract. Results presented in the following show structural analysis of metal-oxide surfaces and the extraction of physical quantities from the force field above such a surface by noncontact atomic force microscopy (NC-AFM). The measurements have been performed with our dual mode NC-AFM/STM in ultrahigh vacuum at 5 K. The introduction will be followed by a description of the experimental setup, including the ultrahigh vacuum cryogenic environment and our tuning fork tunneling current and force sensor. The sensor parameters affecting the measurements are given together with an amplitude characterization method. In the next section, a structure determination of ultrathin Alumina/NiAl(110) is shown. Atomic resolution could be achieved throughout both reflection domain unit cells. NC-AFM reveals details of morphological features, interconnections to substrate–film interactions, and comparability to theory also with respect to topographic height. In the last section, we present measurements beyond imaging, namely spectroscopy data taken on thin MgO films grown on Ag(001). Force–distance measurements based on atomically resolved NC-AFM images of these films have been taken. Inequivalent sites could be resolved and their effect on nucleation and adsorption processes is considered. Furthermore, work function shift measurements on different MgO film thicknesses grown on Ag(001) are studied and the impact of this shift on the catalytic properties of adsorbed metal species is discussed.

7.1 Introduction

In the last few years, it has been demonstrated that noncontact atomic force microscopy (NC-AFM) can be the bridge to nanoscale science on insulating surfaces in general and metal-oxide surfaces in particular. Our work is focused on examples of the latter. Atomic resolution imaging of oxide surfaces gives access to their structural details including, atomic positions, point and line defects as well as to their morphology within certain limits. Additionally, the specific nature of the interaction that enables force microscopy permits the study of physical and chemical material properties of samples and tip–sample combinations, respectively. This may be possible down to the atomic level

depending on the measured quantity and is achieved by the examination of the force field between tip and sample in one, two or three dimensions, which are lines, planes, and volumes above the surface. Contact potential difference, charging, and comparative chemical identification are just three examples that can be addressed with this quickly developing class of techniques. Fortunately, they can be implemented in just one experimental setup. With this, the desired comparability among the techniques and to theory can be facilitated even on a quantitative level. Further, the development of functionalized tips and defined oxide surfaces offers great freedom in the study of surface processes. Such knowledge provides a toolkit for surface science and especially surface chemistry where NC-AFM can be involved in the study of structure, adsorption, initial growth, as well as reaction mechanisms and dynamics on oxide surfaces, for example, in the interesting field of model catalysis. Paramount questions in that field are the nature, vitality, and structure of the proclaimed "active sites" and their selectivity mechanisms in heterogeneously catalyzed chemical reactions. The fundamental interactions of metal atoms, clusters, and molecules with metal-oxide supports studied in this context are in fact relevant to several technological fields. An understanding of growth mechanisms and parameters of the respective geometric and electronic structures are of huge importance [1].

Atomic resolution has been a focus of scanning probe methods for the last two decades. With our low temperature microscope, we have achieved atomic resolution in NC-AFM and in the scanning tunneling microscopy (STM) mode. This includes the small and highly symmetric unit cell of the thin MgO(001) on Ag(001) as well as the two large and complex reflection domain unit cells of the thin alumina overlayer on NiAl(110) with its site distances comparable to those on closed packed metal surfaces.

Our results obtained for the Alumina/NiAl(110) surface shed light on a recent density functional theory (DFT) model from a new angle and show that NC-AFM is capable of giving new insight and different perspectives on experimental and theoretical results obtained with other techniques. In particular, results different from STM are shown, which spark interest in similarity and complementarity of results from both methods. The mapping and study of samples like complex oxide surfaces with densely packed sites require extreme stability and high sensitivity if one is to reach sub-Ångström spatial and adequate force resolution. In recent years, there have also been considerable efforts towards clarification of how to handle individual frequency shift curves that vary depending on the microscopic tip and of how to best extract unbiased results from these data. In this context, new in situ amplitude characterization techniques emerged during our studies [2]. However, providing the ultimate level of understanding requires developments in NC-AFM itself.

Atomic resolution on MgO/Ag(001) as well as the small unit cell are perfect starting points for measurements beyond imaging. For example, a detailed force field analysis revealing physical information of different sites is of great interest in catalysis especially for adsorption experiments. The chemical

activity of adsorbed metal particles depends strongly on their charge. Neutrally deposited Au atoms on MgO films might in some cases be charged and thus become chemically active [3]. Since a shift in the metal work function turns out to be the key factor for the charge transfer, we determined this shift with our dual mode NC-AFM/STM.

At this point, a comment may be necessary. In our publications, we use the nomenclature frequency modulation dynamic force microscopy (FM-DFM) for the FM mode in NC-AFM. It displays the implemented method and identifies it as a dynamic technique in contrast to the static bending of the first atomic force microscopes [4]. The historic notion of noncontact, however, can lead to conceptual difficulties when analyzing the details of the imaging mechanisms and to confusion between different implementations of force microscopy. Nevertheless, it has to be acknowledged that the word NC-AFM has gained a huge uniting power in the field of force microscopy, bringing together such different areas as biological studies under physiological conditions and works on single crystals at cryogenic temperatures with atomic resolution. We therefore think that the title for this book is not only well chosen, but that it has an appealing sound to it. In the following, we use NC-AFM synonymously for FM-DFM.

7.2 Methods and Experimental Setup

Our instrument (Fig. 7.1) is optimized for high resolution imaging in both NC-AFM and STM. The microscope operates in ultrahigh vacuum (UHV) at cryogenic temperature (5 K), which reduces damping of the force sensor and enhances it with respect to tip stability as well as to reduction of thermal drift, piezo creep, and piezo hysteresis. The setup ultimately enables atomic-resolution imaging and ultrastable spectroscopy of conducting and insulating surfaces by recording tunneling current and frequency shift with the same microscopic tip and if desired at the same time. Besides detailed investigation of surface structures, the high stability allows site-specific spectroscopy measurements, atom transfer, and single adatom contacts to be performed. However, meaningful conditions for such measurements can best be achieved at cryogenic temperatures. Therefore, evaporation of metals onto samples at low temperature is implemented beside the standard facilities for metal crystal and oxide film preparation. All measurements presented in this chapter were performed in UHV at 5 K [5]. More details on the particular equipment can be found in [5–7].

7.2.1 Quartz Tuning Fork-based Sensor for Dual-Mode NC-AFM/STM

The sensor in use is a quartz tuning fork as presented in [8] with a cut Pt/Ir wire as a NC-AFM/STM tip (see Fig. 7.2). Tip preparation can be performed in situ by field emission and/or dipping the tip into and pulling necks from
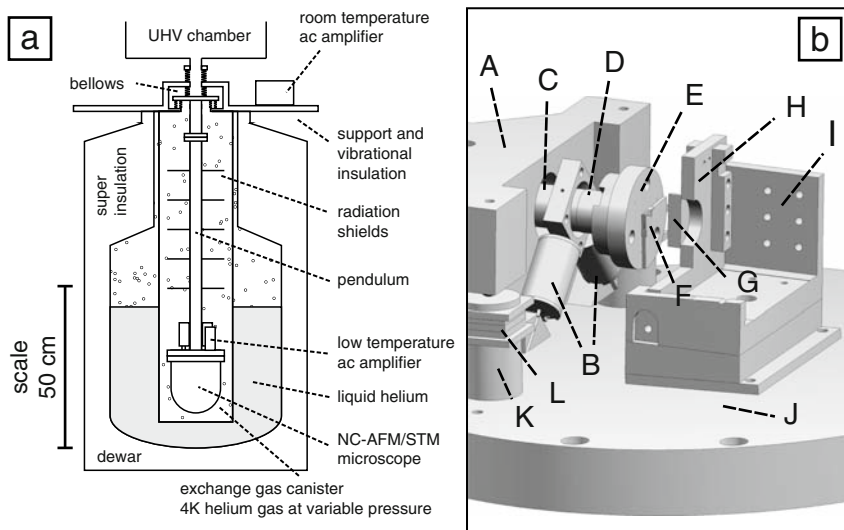
Fig. 7.1. (**a**) The experimental setup. An evacuated pendulum of about 1 m length suspended with steel bellows from the main UHV chamber is the central design feature for providing mechanical vibration insulation for the microscope. At its end, the NC-AFM/STM head is mounted in an UHV environment. The pendulum is placed inside an exchange gas canister filled with helium gas, which is surrounded by a liquid helium bath. The helium gas chamber prevents acoustic noise from perturbing the microscope while permitting thermal coupling to the liquid cryogen (helium or sometimes nitrogen). The low temperature ac amplifier is situated near the NC-AFM/STM head while the room temperature ac amplifier is mounted outside the dewar. (**b**) The microscope on its support stage: (A) Walker unit, (B) x-, y-piezo and (C) z-piezo of the tripod scanner unit, (D) z dither piezo, (E) sensor carrier, (F) tuning fork assembly, (G) sample (not fully drawn), (H) sample holder (not fully drawn), (I) sample stage, (J) microscope stage, (K) walker support, and (L) shear stack piezos. The support stage has a diameter of 100 mm

the sample surface. This removes residual oxide contaminants, produces good tip configurations, and has proven to be particularly useful with respect to the time consuming handling of UHV and low temperatures. The tuning fork assembly and electronics are capable of simultaneous recording of tunneling current I_t and frequency shift Δf while controlling the z-position of the tip via either of them [7]. The tip–wire has a diameter of 250 μm and is electrically connected to the signal electronics through a thin Pt/Rh wire with a diameter of 50 μm. Both, tip and contact wire are electrically insulated from the tuning fork and its electrodes. The frequency shift is directly recorded via the tuning fork electrodes while the tunneling current is taken independently from the contact wire of the tip (Fig. 7.2). Excitation of the tuning fork along the tip axis is done with a separate slice of piezo (dither piezo) on top of the z-piezo. The force sensor parameters spring constant $k \approx 22{,}000\,\text{N}\,\text{m}^{-1}$, resonance
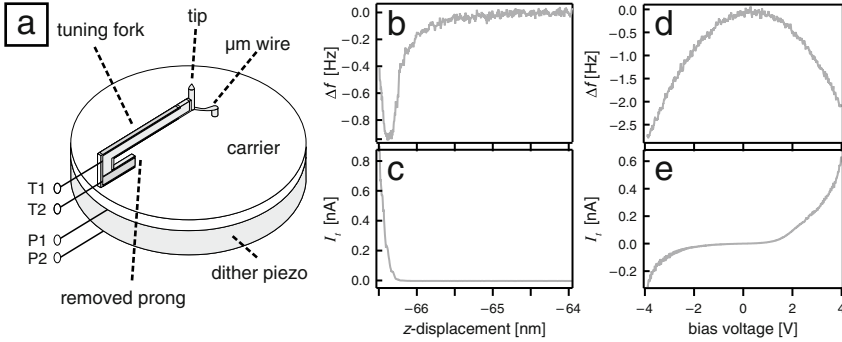
Fig. 7.2. (**a**) The sensor setup for NC-AFM and STM operation in UHV at low temperatures: dither piezo with connections P1, P2 for mechanical excitation in z-direction along the tip–axis. Quartz tuning fork on a ceramic carrier plate. Electronically separated signal wires for force (T1, T2 contacts of the tuning fork) and current (μm wire) detection. The same tip senses both signals. (**b–e**) Pairs of simultaneously recorded signal curves from the frequency shift and the current channel: (**b–c**) Signal–distance curves at constant bias voltage, (**d–e**) signal–bias voltage curves at constant height

frequency $f_0 = 17$–22 kHz, quality factor $Q = 8{,}000$–$25{,}000$ depend on the individual tuning forks. The oscillation amplitude A_{osc} has been set to values within the range 1–20 Å. The spring constant of the tuning fork sensor is significantly higher than typical interatomic force constants. This prevents a sudden "jump-to-contact" of the cantilever even at very small tip–sample distances and oscillation amplitudes. Also, the often observed instability and breakdown of oscillation amplitude after contact formation in the repulsive regime is reduced.

The great advantage of this setup is the simultaneous data acquisition from frequency modulation (FM) force detection in combination with the tunneling current. This enables, for example, the detection of insulating contaminants on the tip via a shift of the NC-AFM signal to larger distances off the surface with respect to the I_{t} signal than without such contaminants. In general, it is interesting to measure the two signals as they may complement each other, and the use of the very same microscopic tip enables direct comparison. A pair of curves from both channels recorded in a sweep in z-direction and another one recorded at varying bias voltage are shown in Fig. 7.2. The sensor is operated by the sensor controller/FM-detector easyPLLplus from Nanosurf [9] in the self-exciting oscillation mode [10] at constant oscillation amplitude. The detected oscillation amplitude signal is fed into an automatic gain control circuit and is used to self-excite the quartz tuning fork mechanically by the dither piezo. A phase shifter ensures that the spring system is excited at its resonance frequency. This operation mode of constant oscillation amplitude allows even to probe the regime of strong repulsive force in contrast to an operation mode at a constant excitation amplitude, where the oscillation amplitude decays

as the vibrating tip penetrates the repulsive interaction regime [11]. It furthermore readily facilitates theoretical analysis of the technique and results obtained with it. An additional custom-built analog FM detector has been used for the frequency shift recording based on [12]. The signal electronics has been described in [7]. A unit by Nanotech Electronics [13] as well as one by Nanonis [14] have been used for scan control and data acquisition.

7.2.2 Concepts for Force and Energy Extraction and Sensor Characterization

For the proper interpretation of tip–sample interaction forces and energies in NC-AFM, one naturally needs to make efforts in their precise extraction from experimental frequency shift data. Formulas (7.1) and (7.2) from [15] allow a determination of tip sample force F and potential energy U from the frequency shift. They are valid for the entire oscillation amplitude range accessible to sensors, that is, large and small amplitude regimes, and also cover the intermediate amplitude range below 1 nm in which we operate our tuning fork. The expression for the force in terms of the frequency shift is given by

$$F(D) = \frac{2k}{f_0} \int_D^\infty \left(1 + \frac{A_{\mathrm{osc}}^{1/2}}{8\sqrt{\pi(z-D)}} - \frac{A_{\mathrm{osc}}^{3/2}}{\sqrt{2(z-D)}} \frac{\mathrm{d}}{\mathrm{d}z} \right) \Delta f(z) \, \mathrm{d}z, \quad (7.1)$$

where D is the distance of closest approach between tip and sample, z is the tip–sample distance, A_{osc} the oscillation amplitude, k and f_0 the sensor constants, $\Delta f(z)$ the recorded frequency shift, and $F(D)$ is the interaction force between tip and sample. Integrating equation (7.1) gives the corresponding expression for the interaction energy $U(D)$ between tip and sample

$$U(D) = \frac{2k}{f_0} \int_D^\infty \left(z - D + \frac{A_{\mathrm{osc}}^{1/2}}{4} \sqrt{\frac{z-D}{\pi}} + \frac{A_{\mathrm{osc}}^{2/3}}{\sqrt{2(z-D)}} \right) \Delta f(z) \, \mathrm{d}z. \quad (7.2)$$

However, other formulas for the large and small amplitude limits, respectively, have already existed earlier [16, 17]. Equation (7.1) shows the dependence of derived force data on the frequency shift and equally important the dependence on sensor parameters. In particular, the oscillation amplitude assumed for force calculation from $\Delta f(z)$ has a crucial influence on the derived force and energy curves, while resonance frequency and spring constant of the sensor are simply proportionality constants. Therefore, we have developed methods for cantilever parameter determination for force sensors with an emphasis on in situ oscillation amplitude determination [2] and evaluated a standard measurement procedure for the spring constant with respect to our much stiffer tuning fork sensor with its particular geometry. For UHV

operation, but also in general, it will be beneficial to have a sensor characterization at hand that can be performed in situ and most important without damaging the microscopic tip. Our proposed amplitude characterization methods rely therefore on characteristics of the tip–sample interactions in frequency modulation NC-AFM or STM and the general response of sensors to them. They can be performed without laser interferometry, which may be desirable in low cooling-power cryostats. The first hurdle towards proper characterization is actually the determination of relative or possibly absolute distances. Relative motion is commonly quantified with monoatomic steps on several clean calibration specimens like low index metal surfaces. Access to absolute values may be achieved (if the sensor permits) via monitoring the conductivity within the tip–sample gap and transferring this to the force channel. For the amplitude determination schemes presented here, only relative positioning is relevant and z-calibration is assumed to be done.

The spring constant determination follows the well known Cleveland method, where frequency changes upon attachment of test masses allow determination of the spring constant from linear regression [18]. For tuning forks, one has to consider the influence of the elastic bearing of the oscillating prong at the base of the tuning fork. It effectively extends the prong into the basis leading to lower values of k than predicted by calculations based on prong geometry. Many other methods, like the static deflection methods, play no role because static deflection of the stiff tuning forks by calibration devices yields too small deflections and does not seem reasonable.

The oscillation amplitude A_{osc} of a tuning fork force sensor or other force sensor can be determined in situ from the characteristic change of signal–distance curves for a measured quantity upon amplitude variation at large amplitudes. The signal of choice can be the average tunneling current $\langle I_{\mathrm{t}} \rangle$ as well as normalized frequency shift γ, frequency shift Δf or its derivative $\Delta f'$. Upon stabilizing the sensor and tip in the vicinity of the sample surface, a set of force– or current–distance curves is recorded at various oscillation amplitudes. A plot of the cantilevers changing relative equilibrium positions at constant $\langle I_{\mathrm{t}} \rangle$, constant Δf, constant γ, or constant $\Delta f'$ vs. the corresponding values for A_{osc} gives the calibration curve. Alternatively, the calibration curve can be recorded by sweeping the amplitude and recording z-displacement while keeping the signal, then typically $\langle I_{\mathrm{t}} \rangle$ or Δf, at a constant value. During the procedure, no tip changes must disturb the measurement. Important for amplitude determination are the larger values of A_{osc}, while the calibration factor is valid also at intermediate or small A_{osc} as long as the deflection varies linearly with excitation. The reason for this is the direct linear correspondence between amplitude increase and change in the sensor's equilibrium position in the large amplitude regime. It has unity slope. This holds, because from a certain value of A_{osc}, the signal interaction occurs solely in the half-period during which the tip is closest to the sample, while the half-period away from the surface gives vanishing contributions. This is the case for all A_{osc} at a constant signal value for which the equilibrium position of the sensor already resides in

the flat curve section of the measured quantity. Any further increase of A_{osc} at a certain equilibrium position then means a deviation from the preset constant signal value, which can then obviously be compensated by a retraction of the sensors equilibrium position that equals the initial increase of A_{osc} in size. Thus one can expect unity slope for the z-displacement of points at constant signal plotted over the A_{osc} they have been recorded with – at least in the large amplitude region. Relating the experimentally determined slope to unity gives the calibration factor for A_{osc}. What amplitude size can actually be considered large depends on the quantity used for characterization and the error that is accepted by the experimenter [2]. Performing the calibration with $\langle I_t \rangle$ or $\Delta f'$ at oscillation amplitudes of several nanometers gives theoretical errors for the calibration factor of a few percent. Therefore, amplitude measurements of reasonable quality are feasible.

7.3 Atomic Resolution Imaging

After years of significant improvements in NC-AFM and after atomic resolution has been obtained on metal, semiconductor, and insulator surfaces [19–22], insulating surfaces with larger and much less symmetric unit cells are being studied. However, the amount of data from these systems is still very limited. Recent work on bulk alumina or associated thin films on NiAl and Ni$_3$Al surfaces has been promising though [23–27]. Being the very basis for more detailed insight into physical and chemical properties of a surface by NC-AFM, atomic resolution needs to be extended further towards more complex surface unit cells, larger corrugations (steps, kinks, molecules), and to bulk samples. Progress on thin films can be considered as a stepping-stone towards resolving all positions in large complex reconstructed surface unit cells of bulk insulators. Our sample system, the ultrathin alumina film on NiAl(110), with its high density and large number of inequivalent surface sites constitutes a good test for the resolution of our ultrahigh vacuum, low temperature NC-AFM. We present detailed images of the complex microstructure for both reflection domains of the thin alumina obtained with our microscope [28]. Resolution is such that atomic positions can be determined by simple graphical analysis in real space without application of filtering or correlation methods, emphasizing the potential of NC-AFM on complex oxide surfaces (Fig. 7.3).

Thin (5 Å) crystalline alumina overlayers can be grown on (110) surfaces of the ordered (CsCl-structure) intermetallic compound NiAl [29]. Film preparation has been carried out according to the recipe presented in the literature [29,30] and resulted in the usual flat topography with long range order on extended terraces and reflection as well as antiphase domain boundaries. Despite a large bandgap of about 6.7 eV [31], the limited thickness allows electron flow through the film into the substrate and therefore the application of electron based analysis techniques. Extensive studies in the context of model catalysis with many such surface science techniques [29–38] and a recent STM
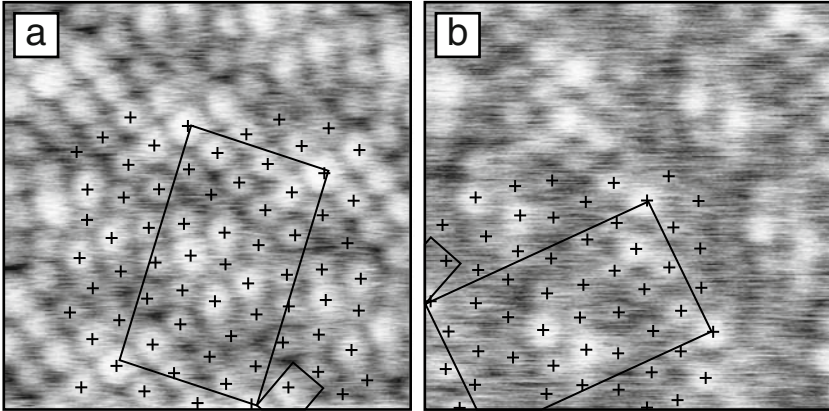
Fig. 7.3. High resolution NC-AFM images of the ultrathin alumina film on NiAl(110). (**a**) Domain B, (**b**) domain A. The geometrical relation between the oxide and the small NiAl(110) surface unit cell as well as overlays of atomic positions with crosses are indicated. Images were leveled and equalized. Scan area $3 \times 3\,\mathrm{nm}^2$ each. (**a**) $\Delta f = -6.2\,\mathrm{Hz}$, $A_{\mathrm{osc}} = 1.4\,\text{Å}$; (**b**) $\Delta f = -6.7\,\mathrm{Hz}$, $A_{\mathrm{osc}} = 1.7\,\text{Å}$

and DFT study converged into an atomistic model of the film that matches many of the experimental findings [39]. The accumulated data give so far evidence for a nickel-free structure with two aluminum and oxygen double layers. It is oxygen terminated towards the vacuum with the next lower layer of 24 aluminum atoms 40 pm underneath. This aluminum layer sits on top of an oxygen interface layer with the equal number of 24 atoms. The bottom-most layer accommodates 16 aluminum atoms and anchors the film to the substrate. Lattice constants of the film's large, slightly parallelogram-shaped surface unit cells as determined by low energy electron diffraction are $b_1 = 10.55\,\text{Å}$ and $b_2 = 17.88\,\text{Å}$ enclosing an angle $\alpha = 88.7°$. Each oxide surface unit cell covers 16 of the $2.89 \times 4.08\,\text{Å}^2$ sized rectangular NiAl(110) surface unit cells. Dimensions, geometry, and orientation between the two oxide reflection domains and the substrate are illustrated in Fig. 7.4c. However, because of technical constrains, the DFT model [39] assumes a commensurate structure (10.93 Å, 17.90 Å; $\alpha = 88.16°$) for the film which is incommensurate in the [001] direction of the NiAl substrate. Extreme tunneling conditions in underlying STM data for the topmost oxygen layer give rise to speculations over substrate influence, mixed contributions from different atomic layers to images assigned to only one layer, and force interactions in the images. Therefore, the atomic surface structure is still under discussion and more real space information with atomic resolution is desirable.

Low noise, as achieved by low temperature pre-amplifiers, all measures for mechanical and electrical noise reduction, operation in UHV and at low temperature, is self speaking a fundamental prerequisite for highest resolution and stability. Another is a common set-point for the frequency shift across the
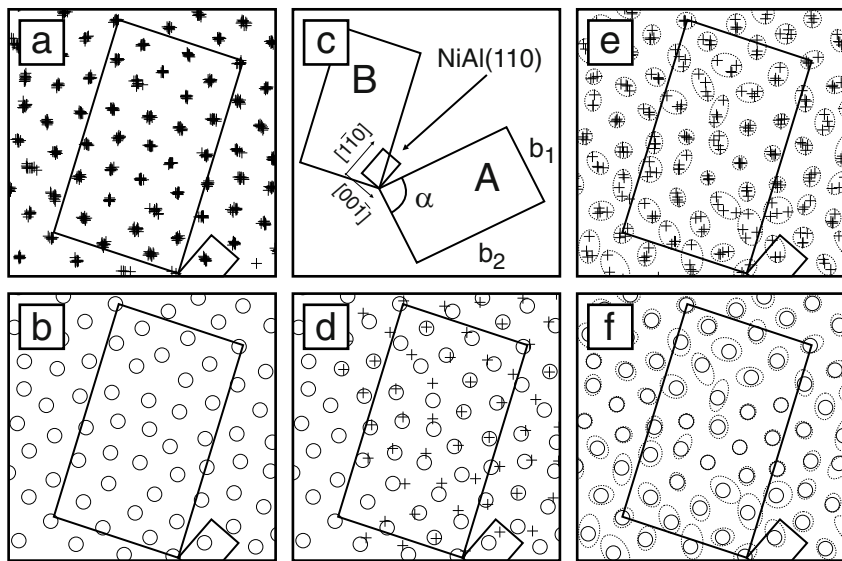
Fig. 7.4. (**a**) Stack of ten superimposed overlays with crosses of the surface unit cell taken from NC-AFM image in Fig. 7.3a of domain B. The spread in each set of crosses indicates the uncertainty due to imaging noise, weak contrast, and reading errors. (**b**) Average for overlays from (**a**) being the mean positions of the groups of crosses. (**c**) Geometry and dimensions of the two oxide overlayer domains A and B, their orientation relative to each other and to the NiAl(110) substrate ($b_1 = 10.55$ Å, $b_2 = 17.88$ Å, $\alpha = 88.7°$). (**d**) Average positions of domain A (*crosses*) reflected onto result for domain B (*circles* from (**b**)) for comparison. (**e**) Positions for the averaged overlays of several images (domain B). The spread here (given by *dotted loops*) allows to check reproducibility. (**f**) Average of positions from (**e**)

surface structure, which gets increasingly difficult with stronger corrugation and dissimilar interaction atop different sites. Large terraces reduce problems with features outside the scan frame and also small amplitudes have turned out to be advantageous. Last, but not least, one is to address the tip with the inherent uncertainties around its structure, stability, and chemical composition. Recorded surface structures have to be verified with another microscopic tip in each case. In our scheme, this is facilitated by in situ preparation of the tip with field emission and/or dipping (see Sect. 7.2.1).

Atomic resolution NC-AFM images of the ultrathin alumina film on NiAl(110) are shown in Fig. 7.3. Several such images of both the film's surface unit cells have been obtained. They have been leveled (subtraction of a parabola from each line in the image) and equalized (selected height range to enhance the image contrast), but no filtering has been necessary. However, long acquisition times required minor lateral corrections to be performed to account for slight drift. Clearly resolved are 28 individual protrusions visible in the surface unit cell of each reflection domain. This is in agreement with

the number of oxygen sites in the topmost layer of the DFT model and differs from the predicted number of 24 aluminum atoms in the second layer, which is in line with earlier experimental data on oxygen termination of the film. To show that the lateral structure is reproducibly obtained from the images, the following has to be confirmed:

- Scattering of positions related to reading error, noise, and reduced contrast in the images has to allow separation of all protrusions within each image.
- Lateral spread among positions of protrusions from different images assigned to the same site has to allow separation from all other sites. Here images should be recorded with different tips to guarantee reproducibility.
- A structure derived for one domain has to match the mirror image of the respective reflection domain.

To check the images for these requirements, they have been evaluated with respect to bright protrusions (Fig. 7.4). After identification of an identical surface unit cell in all images of both domains, overlays of the observed protrusions with crosses have been produced. Several overlays for the same image give a measure for the statistical reading error and uncertainty due to noise and weak contrast, while a comparison of overlays from different images (recorded after tip change or tip preparation) gives an idea of the imaging contribution and condition, that is, scanning parameters, shape, and atomic composition of the tip as well as atomic contrast mechanisms, to the uncertainty in position. Recurrent structures from such different and independent images indicate therefore reproducibility. The average positions in both cases are taken as mean positions of the sets of crosses belonging to individual positions in different overlays. Average overlays are shown in Fig. 7.4(b, d, f). The rather regular shapes of the areas covered by the groups of crosses belonging to the individual and averaged positions in different images – as given by dotted loops – emphasize that the found overlays are quite well defined (Fig. 7.4(e, f)). Most of the positions can be distinguished without any doubt. The evaluated images, which have been recorded with different microscopic tips on different surface sites, show that equal patterns and reproducibility are established. This is supported by the finding that the structure in one domain is reproduced by the mirrored positions from the other reflection domain (Fig. 7.4(d)), as required.

Each surface unit cell contains 28 observable protrusions matching the number proposed for the topmost oxygen layer by the DFT model. Figure 7.5 shows a direct graphical comparison with that oxygen layer of the model given in the supplement to [39]. We find the similarity rather striking. To first approximation, they indicate individual atomic sites marked with crosses in Fig. 7.3. One can also see that positions interconnecting the characteristic squares and rectangles of eight oxygen sites in the model are among the brightest protrusions in the NC-AFM images. On the other hand, protrusions at points with lower contrast naturally exhibit larger scattering of the crosses in Fig. 7.4e. These points fall into the troughs of the wave-like feature visible
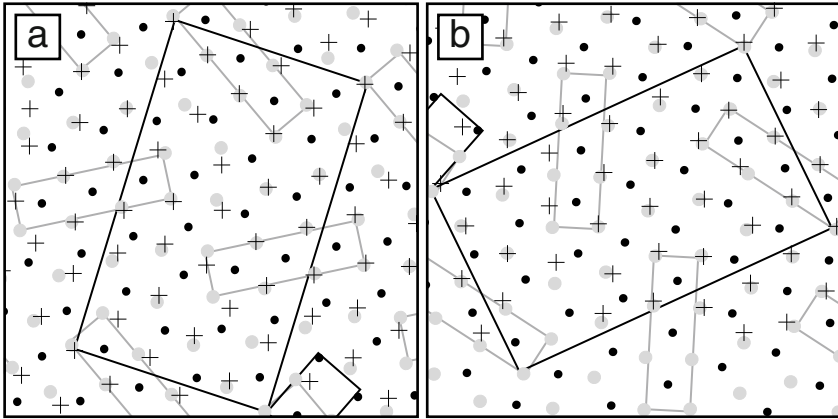
Fig. 7.5. Comparison of the atomic positions from averaged overlays for both domains (*crosses*) with those of the topmost oxygen (*grey dots*) and aluminum (*black dots*) atoms in the DFT model. Large black parallelograms indicate the oxide unit cell as chosen already in Fig. 7.3. Attached is the small black rectangle of the NiAl(110) unit cell. *Grey rectangles* highlight characteristic blocks of 8 surface oxygen atoms in the model. (**a**) Domain B, (**b**) domain A

in NC-AFM images (Fig. 7.3 and 7.6). It consists of alternating bright and dark rows: crests and troughs. This wave-like topography of the surface unit cells is in fact typical for the film [40] and related to strain and commensurability [41, 42]. As observed by NC-AFM before [24], the crests are 9 Å apart but the full repeat unit has a length of 18 Å, that is, that of an oxide unit cell. Each two of the protruding rows differ slightly in apparent structure, height, and contrast, making them inequivalent as shown in Fig. 7.6. However, a row pairing in lateral direction has not been found.

As the lateral structures can be resolved, the topography of the characteristic rectangular arrangements of eight oxygen atoms has been evaluated in detail (Fig. 7.7). The two opposing rectangular arrangements in the surface unit cell should be laterally equivalent due to the glide mirror plane in the structure's symmetry. With respect to average height and corrugation, however, they could differ. And indeed one sees a different spread in z-direction for the eight oxygen sites on inequivalent crests. This can be seen from each two parallel rows of four protrusions within the two opposing blocks. They are contrarily inclined with respect to each other. This is shown in Fig. 7.7 and compared with height values for the calculated oxygen sites of the DFT model. The experimental data are in reasonable qualitative and quantitative agreement with the theoretical result. Also, the DFT coordinates exhibit a mean height that is 6 pm smaller for the eight oxygen in the less pronounced crests compared to the stronger crests. In agreement with this, one finds a difference in mean height of 2.5 pm between inequivalent crests. If one now
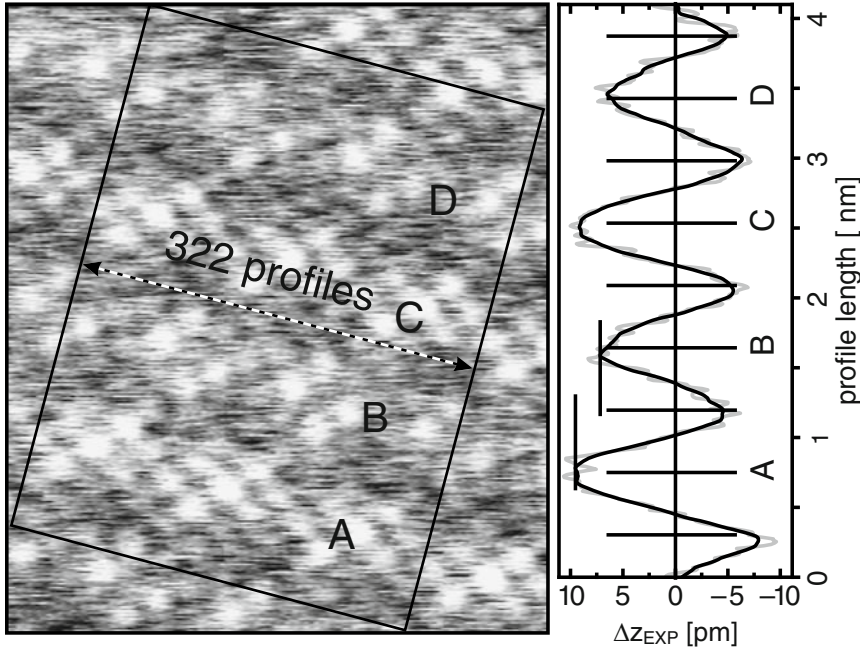
Fig. 7.6. NC-AFM image of a B domain (scan range $4.1 \times 4.8\,\mathrm{nm^2}$, $\Delta f = -5.5\,\mathrm{Hz}$, $A = 1.4\,\text{Å}$). The wave-like topographic feature of the oxide film exhibits two inequivalent but equidistant crests. They differ in the arrangement, contrast, and number of their brightest protrusions. The length of a complete period of the feature is 18 Å. The right part shows an average of 322 line profiles (*grey curve*) lined up along the short end (indicated by the *dashed double arrow line*) of the three unit cells broad rectangle marked in the image. The *black curve* has been smoothed. Every second crest is less pronounced. Line segments in the line profile are set to spacings of a quarter of a unit cell length

considers the orientation of these oxygen blocks with respect to the substrate, one finds those on the more pronounced crests to be rotated about 7° off the NiAl[001] axis. A similar result has been found for short gold chains adsorbed at low temperatures onto this film system. Their alignment at about 5° off the NiAl[001] symmetry axis results from a minimization of the mismatch towards the surface aluminum rows of the oxide film as well as to those of the substrate [43, 44].

Results in the lateral directions are consistent with a published density functional theory model and connect directly to other experimental data from the literature. For two prominent structural features, agreement with theory is found even for topographic height. Results reveal that structural analysis with sub Ångström resolution can allow insight into details beyond the atomic surface arrangement itself.
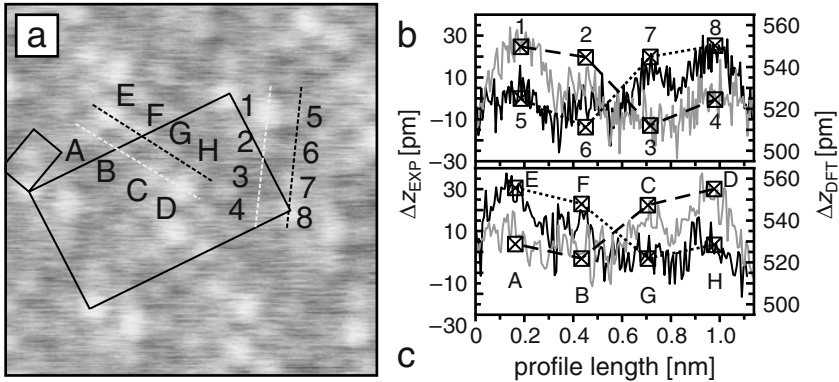
Fig. 7.7. (**a**) Topography of rectangular blocks of 8 protrusions. Scan range $3 \times 3\,\text{nm}^2$. The parallel rows of four positions are inclined in opposite directions along the rectangle. (**b**–**c**) Line profiles in comparison to absolute heights for corresponding oxygen positions from the DFT model (*boxes with crosses*)

7.4 Beyond Imaging: Spectroscopy

In this section, we focus on site-specific spectroscopy measurements. Here we benefit from the great advantage of the dual mode NC-AFM/STM capabilities. The ability to sensitively detect forces as well as the local density of states with spatial resolution down to the atomic scale, at the same position and at the same time, is of great interest, as forces and effects related to electronic structure are fundamental quantities in physics. Concepts for force and energy extraction and sensor characterization are provided in Sect. 7.2.2. In the NC-AFM mode, the detected tip–sample force interaction can be used to generate a laterally resolved image (see Sect. 7.3) or to determine its distance dependence (see Sect. 7.4.1). During these measurements, the tunneling current is mapped simultaneously. The term spectroscopy might be irritating as it is usually related to energies and not to distance dependencies. Nevertheless, we will use it throughout the text, because it is somehow established in this sense throughout the literature. The basic parameters that can be varied in the experimental setup are the lateral and vertical displacement in x-, y-, and z-direction, the sample voltage V_s, and the oscillation amplitude A_{osc}, while measuring the frequency shift Δf, A_{osc}, dissipation, and the tunneling current I_t.

A wide variety of physical questions has been tackled with the help of scanning tunneling spectroscopy (STS) on its own. It provides the possibility to study electronic effects on a local scale. The analysis of Landau and spin levels [45], vibrational levels [46], Kondo resonances [47] as well as the imaging of electronic wave functions, like Bloch waves [48], drift states, and charge density waves [49], are only a few examples. As STS reflects the sum of squared wave functions, it is an obvious task to measure the local appearance of such

wave functions on solid surfaces. The combination of NC-AFM and STM provides therefore an extremely powerful tool to study local effects on oxide film surfaces.

For the spectroscopic measurements in this section, it seems useful to change the sample system from the complex surface structure of the thin alumina film to the rather simple structure of MgO films. Presented are a few topics and exemplary results performed with our setup on thin MgO(001) films deposited on Ag(001), which aim at characterization of properties of a certain area on the sample surface. The oxide film has been investigated with our STM and STS capabilities in the context of the analysis of localized electronic defects. Depending on the location (kink, edge, corner) of the defect, for the first time different defect energy levels have been observed in the band gap of MgO. The charge state of defects has been shown to be manipulable by the STM tip. Comparison with ground state energy levels of color centers on the MgO surface obtained from embedded cluster calculations supports the assignment of the defects to singly and doubly charged color centers [50].

Furthermore, adsorption properties of single gold and palladium atoms have been explored with respect to the thickness of supported MgO films underneath [51]. For Au on different MgO film thicknesses (3 and 8 ML), significant differences in the distribution of Au adsorption sites and in the Au cluster geometry have been found, which are in line with recent calculations and electron paramagnetic resonance experiments. On the surface of thick MgO films or unsupported MgO, Au adsorbs on O sites [52], and the equilibrium cluster geometry is three dimensional. In contrast, the calculations performed for thin MgO films predict a change of the preferred Au nucleation site [53] and a stabilization of two-dimensional Au cluster geometries [54]. While Pd atoms are arranged in a random fashion, Au forms an ordered array on the surface. The long-range ordering as well as the STM appearance of single Au atoms on a 3 monolayer thin MgO film can be explained through partial charge transfer from the substrate to Au atoms as predicted recently by density functional theory calculations [53]. In contrast to that, Au atoms on a thick film were found to be essentially neutral.

In the following, we present measurements beyond the imaging capabilities of NC-AFM. In the first section, we show z-spectroscopy measurements on individual atomic MgO sites followed by work function shift measurements on different MgO film thicknesses in the second section.

7.4.1 z-Spectroscopy on Specific Atomic Sites

Here precise measurements at 5 K, where the frequency shift is measured as a function of z and lateral displacement, are presented in detail. From these spatially resolved frequency shift spectra, the interaction force and energy can be directly derived. For the analysis and interpretation of NC-AFM images, it is important to measure the full interaction potential between probe and sample. Instead of keeping the frequency shift constant, it becomes necessary

to map the frequency shift at different z-displacements over the sample surface. Such a type of measurement allows to search for the largest interaction potential and to analyze the variation of the interaction potential at specific surface sites.

Frequency shift vs. distance curves can be measured at specific lattice sites or can be acquired in every point corresponding to a pixel of a NC-AFM image. Different types of modes for the force mapping have already been discussed in the literature for atomic force microscopes under ambient conditions operated in a static mode [55–57]. Measurements of site-dependent frequency shift curves on an atomic scale as a function of the tip–sample surface distance have been reported by several authors, for example, [8,58,59]. Moreover, distance dependent NC-AFM images [60], giving the possibility to acquire three-dimensional force related maps by NC-AFM, have been presented. Complete three-dimensional force fields with atomic resolution by NC-AFM have been shown by Hölscher et al. [61,62], where the force fields have been derived from frequency shift curves aligned at the previously acquired topography image.

Figure 7.8a shows an image with atomic resolution, which has been obtained on a flat terrace of the MgO film. The largest difference in contrast corresponds to adjacent next-neighbor ions in the (010) direction. A schematic illustration of the MgO/Ag(001) growth model is provided in Fig. 7.8b. After acquisition of the NC-AFM image, frequency–distance measurements were performed above the center of the two inequivalent labeled sites (Fig. 7.8d, position 1, 2), which will be discussed later on in more detail.

For the acquisition of two- or three-dimensional force or energy maps, the frequency shift needs to be measured, while moving the oscillating tip in x-, y-, and z-direction over a selected scan field. In principle, it should not matter in which direction one first moves the tip over the scan field. The order is defined by the needed precision in the spatial resolution and drift aspects of the scanner unit. A schematic view of this method is provided in Fig. 7.8c. The three dimensions in x-, y-, and z-direction can be independently addressed. The movement of the tip is adjusted by time synchronized triangular voltage cycles for the different scan directions. Here we have chosen to acquire the data set in the sequence of x-, z-, and y-direction, where x has the fastest and y the lowest scan speed. A single x-, z-scan is marked by a gray shaded area in Fig. 7.8c. With this setup we achieve a very high spatial resolution of the frequency shift in x-, z-direction. Such a frequency shift map is provided in Fig. 7.8d, where the frequency shift is color-coded and plotted across the x-, z-direction. The onset of atomic resolution can be seen by the lateral variation of the potential.

In Fig. 7.8e, a pseudo three-dimensional view of such a data set is plotted to illustrate the measured interaction potential in more detail. The atomically resolved contour lines show the variation in the interaction strength of the tip–sample surface potential. From these data sets, it is possible to derive the
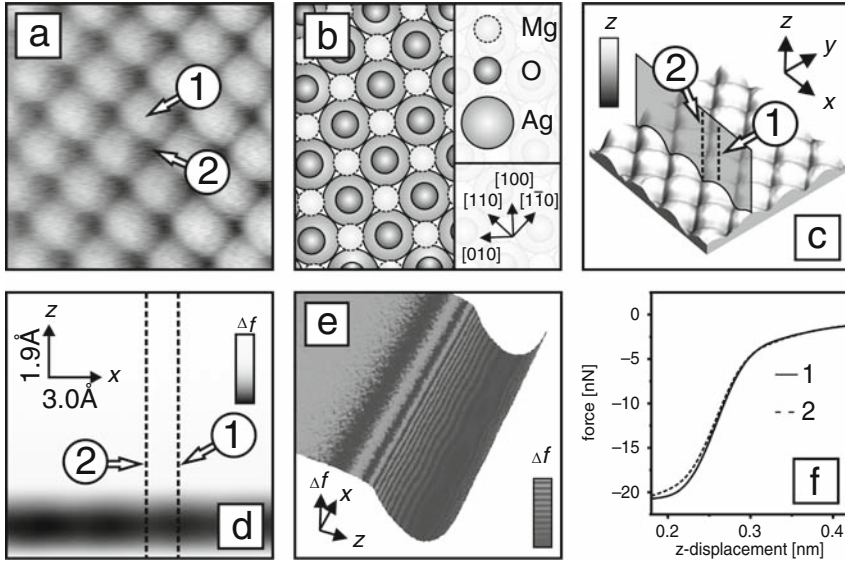
Fig. 7.8. (a) NC-AFM image of MgO on Ag(001) with atomic resolution. Scan area 1.5×1.5 nm, $\Delta f = -8.5$ Hz, oscillation amplitude $A_{\mathrm{osc}} = 0.35$ nm, $T = 5$ K, approximately 30 pm corrugation. The labels 1 and 2 indicate the position of frequency shift distance measurements (see text). (b) The MgO/Ag(001) growth model, schematic illustration of the configuration: Mg-atoms occupy hollow sites, that is, they continue the Ag fcc lattice ($a = 0.409$ nm), O-atoms occupy top sites. Schematic of the NC-AFM spectroscopy method. (c) During the data acquisition, the oscillating tip is moved in x-, z-, and y-direction over the selected scan field. A single x-, z-scan is marked by a *gray shaded area*. (d) Frequency shift image map of the selected x-, z-plane (1.5×0.95 nm). (e) A pseudo three-dimensional view of the frequency-shift measured in the x-, z-direction. (f) Selected force vs. distance curve calculated by the given formula (7.1) from the frequency shift image map at specific lattice sites marked in (c–d)

interaction force F between tip and sample as well as the according energy U by using formulas (7.1) and (7.2) [15].

Figure 7.8f displays two site-specific force distance curves (labeled 1 and 2) calculated from the frequency shift map in Fig. 7.8d. The selected curves are equivalent and in full agreement with single frequency shift vs. distance curves taken at the corresponding surface sites. Beside further quantification, we can now compare the features of the image obtained at a constant frequency shift (Fig. 7.8a) with the site-specific frequency-shift curves (Fig. 7.8f). One type of ion is imaged as a protrusion while the other one is imaged as a depression, which is a typical finding for ionic surfaces imaged by NC-AFM [22,63]. Here, the tip seems to prefer one atomic species. The comparison of the two force distance curves calculated from frequency shift vs. distance curves (Fig. 7.8f) clarifies that the deepest minimum, that is, the strongest tip–sample

interaction occurs at the protrusion. As the electron density on the MgO surface is maximal above the oxygen atoms [64], it is likely that the maxima in the NC-AFM image correspond to the position of the oxygen atoms. Moreover, electron paramagnetic resonance spectra have shown the possibility to determine the adsorption site of Au atoms, namely, adsorption on top of oxygen ions on the terrace of the MgO surface [52]. The hyperfine coupling constants measured by electron paramagnetic resonance spectroscopy are comparable to density functional theory calculations, indicating a good qualitative agreement of the theory with the experimental results. We can now consider a metallic tip apex to correspond to a metal atom or cluster, which probes the sample surface for adsorption sites of equilibrium force or energy interaction. With this measurement characteristics, we have an additional tool, which probes inequivalent surface sites to extract atomic-scale information on surface chemical reactivity and possible adsorption sites for metal atoms and small clusters. The combination with the highly resolved interaction potential in x- and z-direction furthermore allows one to derive the full shape of the interaction potential for further comparison with theoretical calculations.

7.4.2 Work Function Shift Measurements

In this section, we present three independent techniques to determine the metal work function shift of Ag(001) covered by different thickness of MgO films. The influence of the work function shift on charge transfer from a metal support through the thin MgO oxide film to neutrally deposited Au particles will be discussed. Finally, the experimental data will be compared to DFT calculations.

Charged particles and clusters adsorbed on metal supported thin oxide films are of high interest in the research area of catalysis. For example, Au particles that are rather inert become chemically active when they are charged. It has been shown that Au_8 clusters deposited on MgO are active in the $CO + 1/2\,O_2 \rightarrow CO_2$ conversion [3, 65] if stabilized at color centers (two electrons trapped in an oxygen vacancy) providing the charge. A typical defect concentration is about 1% of a monolayer [65], and as a consequence, charge transfer is not as likely as desired for catalytic processes. Recently, Pacchioni et al. [53] proposed charge transfer from a metal support through a thin MgO film to adsorbed Au particles also in the absence of defects [53, 66]. STM measurements in combination with DFT calculations confirmed the charge transfer for Au monomers and dimers adsorbed on defect poor thin MgO films grown on Ag(001) [51, 67]. Charge transfer depends on a variety of different mechanisms and effects. The most important ones are now briefly presented. With increasing MgO film thickness, the tunneling probability decreases. Thus the oxide film thickness must not exceed the tunneling length of the electrons, otherwise the charge transfer is shut off. Therefore, the film thickness might be used as a parameter to tune the catalytic properties of the adsorbed Au as discussed by Freund [68]. Furthermore, the electron affinity of the adsorbed

species should be high. A key factor for the charge transfer is a shift in the metal work function, resulting in a reduction of the tunneling barrier and thus an increase of the tunneling probability. This work function shift results mainly from the metal/oxide bonding distance. The oxide film reduces the surface electron density overspill into the vacuum and thus the surface dipole that the electrons, tunneling from the substrate to the adsorbed particle, have to overcome. This is clearly resolved for MgO/Mo(001) having a seven times larger adhesion energy than MgO/Ag(001), thus resulting in a shorter oxide-metal bond followed by a higher surface electron density compression and consequently a larger work function shift than for MgO/Ag(001) [66]. Moreover, the work function shift depends on metal induced gap states. Such states arise from penetration of metal electron wave functions into the oxide overlayer and from chemical bonds between metal and oxide [69, 70]. To determine the shift in the metal work function of Ag(001) with respect to different MgO film thicknesses, here nominal 0.5 ML MgO (effectively 1 ML MgO islands), 3 ML MgO, and 8 ML MgO (Fig. 7.9(a–c)), we applied three different methods.

The tunneling current as a function of z-displacement of the tip ($I_t(z)$), field emission resonances (FER) as well as contact potential differences (CPD) have been measured at defined lateral tip positions on terraces of the mentioned sample surfaces. While the first two methods are related to the tunneling current, the third method is related to the electrostatic force between tip and sample. Here we benefit from the possibility of our setup to directly switch between the three methods. At this stage, the three methods will be briefly introduced and publications for further reading will be stated, followed by the analysis of the data.

Method 1: $I_t(z)$-spectroscopy

During these measurements, the tip is located laterally at a fixed position. The feedback is off and the tip is moved towards the sample surface. Simultaneously, the z-displacement and the tunneling current are detected. During these measurements, the tip is not oscillated. The tunneling current $I_t(z)$ depends exponentially on the z-displacement as described by Binnig et al. [71]

$$I_t(z) \propto \exp\left(-\kappa \sqrt{\Phi_{ap}}\, z\right), \tag{7.3}$$

where κ is a constant, z is the displacement of the tip perpendicular to the surface, and Φ_{ap} is the apparent barrier height. It is not straightforward to extract the work function from the apparent barrier height as we will discuss later. A typical tunneling current vs. z-displacement curve is shown in Fig. 7.9d. From the slope in the logarithmic plot, we can calculate the apparent barrier height. Because of the fact that the tunneling current shows an exponential behavior, the lateral resolution is quite high. This is also true for the second method.
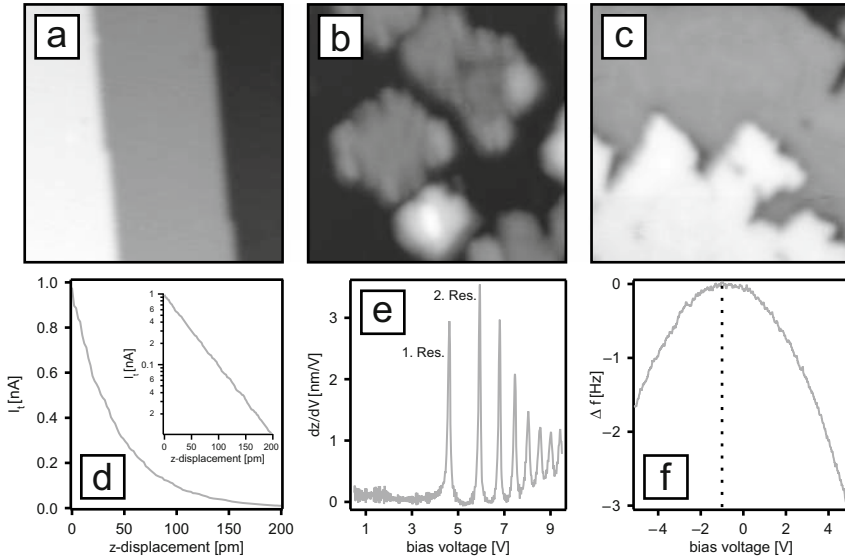
Fig. 7.9. Experiments in spectroscopy modes on top of thin MgO films on Ag(001) with varying thickness. (**a**) Bare Ag(001), $20 \times 20 \, \text{nm}^2$, $V_s = 10 \, \text{mV}$, $I_t = 1 \, \text{nA}$. (**b**) MgO patches (0.5 ML) grown on Ag(001), $50 \times 50 \, \text{nm}^2$, $V_s = 3.5 \, \text{V}$, $I_t = 400 \, \text{pA}$. (**c**) Several layer thick MgO film on Ag(001), $30 \times 30 \, \text{nm}$, $V_s = 3.5 \, \text{V}$, $I_t = 200 \, \text{pA}$. The rotated growth of MgO on Ag(001) is revealed by comparison with (**a**). (**d**) Current distance relation (inset shows the log-plot). (**e**) Field emission resonances on Ag(001). The first two resonances are indicated. (**f**) Parabolic voltage dependence of the electrostatic force component. Offset along the vertical axis due to other force components (subtracted) and along the horizontal axis due to work function difference as indicated by the *dotted line*

Method 2: FER-spectroscopy

Field emission resonances result from interfering electron wave functions. When the applied bias voltage exceeds the work function, electrons can enter a regime between tunneling barrier and sample surface. Electron waves are to some extent reflected at the borders of this regime. As a consequence, standing waves occur representing the eigenstates. The existence of FER was first theoretically predicted by Gundlach et al. [72] and experimentally confirmed by Binnig et al. [73]. To avoid tip changes, which are likely in the constant height mode because of the high electric field when going to high voltages, we measured in the constant current mode with a closed feedback loop. The tip was not oscillating and the lateral position of the tip was constant while the bias voltage was swept (see Fig. 7.9e). For the evaluation of the data, we assumed a 1D trapezoidal potential between tip and sample. Within this approximation, the FER can be described by [74]

$$eV_n = \Phi + \left(\frac{3\pi\hbar e}{2\sqrt{2m}}\right)^{2/3} E^{2/3} n^{2/3}, \qquad (7.4)$$

where e is the charge of an electron, V_n is the voltage of the nth resonance, Φ is the work function, E is the electric field, and n is the number of the nth resonance. This equation does not take the image potential into account. The image potential rounds the corners of the barrier off [72]. Furthermore, the barrier is reduced, resulting in an increase of the tunneling current. As the image potential affects mainly the resonances with small n [74], we did not take the first resonance into account for the evaluation of the data. By fitting equation (7.4) to V_n vs. n, we can determine the work function of the sample system. The work function shift is then determined by the work function difference of the MgO film and the bare Ag(001).

Method 3: CPD-spectroscopy

This method is related to contact potential differences, which can be measured with a NC-AFM. From the collection of different forces acting between tip and sample, the long range electrostatic force is the force of interest, which is given by

$$F_{\mathrm{el}} = -\frac{1}{2}\frac{\partial C}{\partial z}\left(U_{\mathrm{bias}} - \frac{\Delta\Phi}{e}\right)^2, \qquad (7.5)$$

where C is the capacitance, depending on the tip and sample geometry, U_{bias} is the applied bias voltage, e is the charge of an electron, and $\Delta\Phi$ is the work function difference of tip and sample, also known as the contact potential difference. Since the electrostatic forces are always attractive, the resonance frequency shift of the oscillating tip is always negative, see Fig. 7.9f. It shows a parabolic behavior due to the square term in the equation. During the measurements, the x-, y-, and z-position of the oscillating tip were constant, while the bias voltage U_{bias} was swept and the resonance frequency shift was detected (Fig. 7.9f). In this capacitor model involving the tip and sample, there is a vacuum gap when measuring on the bare Ag(001), while in the case of MgO/Ag(001) an additional dielectric is present. This dielectric will change the capacitance between tip and sample and thus it can influence the force between tip and sample, leading to an offset in the resonance frequency shift (Fig. 7.9f offset along the vertical axis). Furthermore, non-electrostatic forces, always present between tip and sample, influences this offset too. As this offset is not carrying the desired information, it can simply be subtracted. The important information arising from the work function difference is the shift of the maximum position of the parabola with respect to the zero bias position, as indicated by the dotted line in Fig. 7.9f (offset along the horizontal axis). By subtracting the work function difference taken on MgO/Ag(001) from the work function difference measured on Ag(001), we can eliminate

Table 7.1. Comparison of experimental and theoretical data [66]

Number of MgO layers on Ag(001)	Theory		Experiment	
		$I_t(z)$	FER	CPD
	$\Delta\Phi$ (eV)	$\Delta\Phi_{ap}$ (eV)	$\Delta\Phi$ (eV)	$\Delta\Phi$ (eV)
MgO island	-1.01^a	-2.0	-1.2	-0.5
3	-1.18	-1.4	-1.4	-1.1
8		-1.2	-1.3	-1.1

[a]Calculated for 1 monolayer

the contribution from the tip and end up with the work function difference between the different MgO films grown on Ag(001) and the bare Ag(001).

Table 7.1 shows the results of the measurements. Column 1 represents the number of MgO layers on Ag(001), column 2 shows theoretical values calculated by density functional theory using the generalized gradient approximation (PW-91 functional) [66]. Columns 3–5 present the experimental data taken with the three presented methods.

As already mentioned, it is not straightforward to extract the work function from the apparent barrier height Φ_{ap}. Controversial statements have been made in the past. Lang [75] claims in his theoretical considerations, a convergence of Φ_{ap} to Φ for large z-displacements, while Chen [76] in his theoretical approach shows that Φ_{ap} stays constant till point contact. The latter has been confirmed by Olesen et al. [77] in an experiment. The apparent work function Φ_{ap} calculated from the $I_t(z)$ measurements shows a large deviation compared to CPD, FER, and the calculated values from DFT. Especially for the MgO islands, Φ_{ap} is overestimated. In the case of the FER, the agreement between experimental and theoretical data is quite convincing. Because of the high lateral resolution, the work function shift derived on the 1 ML high MgO islands is comparable to the calculated DFT values. This high lateral resolution is not available in the third method.

The contact potential difference measurements in the NC-AFM mode on MgO islands reveal a value of $\Delta\Phi = -0.5$ eV. This value seems to be too small compared to the theoretical value of $\Delta\Phi = -1.1$ eV for one monolayer of MgO. The underestimation of this value might arise from a large surface area involved in this measurements, thus the lateral resolution is fairly low, resulting in an average of the bare metal and the MgO patch area. However, this averaging effect seems to have only an influence on patched films and not on closed monolayers of MgO. The work function shift on 3 and 8 ML MgO films turns out to be the same $\Delta\Phi = -1.1$ eV, which is in close agreement with the theoretical predictions.

In conclusion, the analysis, the shift in the metal work function as calculated by Giordano et al. [66] could be confirmed by CPD- and FER-spectroscopy. The agreement between theory and experiment is excellent. As the work function shift is already set up by the first monolayer MgO, the effect seems to be dominated by the metal/MgO interface.

7.5 Conclusion

In summary, these experiments demonstrate different applications, opportunities, and the potential of NC-AFM and combined NC-AFM/STM measurements. For the first time, atomically resolved images of the complex surface unit cells of the ultrathin alumina film on NiAl(110) have been obtained in NC-AFM mode. It has been possible to observe all individual atomic positions in the surface unit cells for both reflection domains of the topmost oxygen layer unambiguously. Our results confirm the combined STM and DFT model [39] and complement earlier NC-AFM images [24] from the literature. For selected structural elements, quantitative agreement for the corrugation has been found. Graphical evaluation of the images and line profiles of spot patterns in the surface unit cell has been sufficient to derive the positions. No application of any filtering or correlation techniques has been necessary. The results are a promising step towards high resolution real space atomistic surface characterization of thick insulating films and eventually bulk surfaces of wide band insulators with complex surface unit cells.

Atomically resolved NC-AFM images of MgO films have been combined with site-specific frequency shift vs. distance measurements. The frequency shift has been measured as a function of z and the lateral displacement [8]. With these measurement characteristics, we have probed inequivalent surface sites on thin MgO films to extract atomic-scale information on surface chemical reactivity and possible adsorption sites for metal atoms and small clusters. Furthermore, the metal work function shift as a key parameter for charge transfer and therefore for the catalytic properties of adsorbed particles has been determined with contact potential differences and field emission resonances spectroscopy. The results are in good agreement with DFT calculations.

Acknowledgements

References

1. H.-J. Freund, Faraday Discuss. **114**, 1 (1999)
2. G.H. Simon, M. Heyde, H.-P. Rust, Nanotechnology **18**, 255503 (2007)
3. B. Yoon et al., Science **307**, 403 (2005)
4. G. Binnig, C.F. Quate, G. Gerber, Phys. Rev. Lett. **56**, 930 (1986)
5. M. Heyde, M. Kulawik, H.-P. Rust, H.-J. Freund, Rev. Sci. Instrum. **75**, 2446 (2004)

6. M. Heyde, M. Sterrer, H.-R. Rust, H.-J. Freund, Appl. Phys. Lett. **87**, 083104 (2005)
7. H.-P. Rust, M. Heyde, H.-J. Freund, Rev. Sci. Instrum. **77**, 043710 (2006)
8. M. Heyde, G.H. Simon, H.-P. Rust, H.-J. Freund, Appl. Phys. Lett. **89**, 263107 (2006)
9. Nanosurf AG, Grammetstrasse 14, CH-4410 Liestal, Swiss.
10. K. Kobayashi et al., Rev. Sci. Instrum. **72**, 4383 (2001)
11. B. Gotsmann, H. Fuchs, Appl. Surf. Sci. **188**, 355 (2002)
12. T.R. Albrecht, P. Grütter, D. Horne, D. Rugar, J. Appl. Phys. **69**, 668 (1991)
13. Nanotec Electronica, Parque Cientifico de Madrid, Pabellon C, campus UAM, Cantoblanco, E-28049 Madrid, Spain.
14. Nanonis GmbH, Technoparkstrasse 1, CH-8005 Zurich, Swiss.
15. J.E. Sader, S.P. Jarvis, Appl. Phys. Lett. **84**, 1801 (2004)
16. U. Dürig, Appl. Phys. Lett. **75**, 433 (1999)
17. F.J. Giessibl, Appl. Phys. Lett. **78**, 123 (2001)
18. J.P. Cleveland, S. Manne, D. Bocek, P.K. Hansma, Rev. Sci. Instrum. **64**, 403 (1993)
19. F.J. Giessibl, Science **267**, 68 (1995)
20. C. Loppacher et al., Appl. Surf. Sci. **140**, 287 (1999)
21. R. Bennewitz et al., Phys. Rev. B **62**, 2074 (2000)
22. C. Barth, C.R. Henry, Phys. Rev. Lett. **91**, 196102 (2003)
23. C. Barth, M. Reichling, Nature **414**, 54 (2001)
24. C.L. Pang, H. Raza, S.A. Haycock, G. Thornton, Phys. Rev. B **65**, 201401(R) (2002)
25. G. Hamm et al., Phys. Rev. Lett. **97**, 126106 (2006)
26. S. Gritschneder, C. Becker, K. Wandelt, M. Reichling, J. Am. Chem. Soc. **129**, 4925 (2007)
27. S. Gritschneder et al., Phys. Rev. B **76**, 014123 (2007)
28. G.H. Simon et al., Phys. Rev. B **78**, 113401 (2008)
29. R.M. Jaeger et al., Surf. Sci. **259**, 235 (1991)
30. M. Kulawik, N. Nilius, H.-P. Rust, H.-J. Freund, Phys. Rev. Lett. **91**, 256101 (2003)
31. S. Andersson et al., Surf. Sci. **442**, L964 (1999)
32. H. Isern, G.R. Castro, Surf. Sci. **211**, 865 (1989)
33. J.-P. Jacobs et al., J. Vac. Sci. Technol. A **12**, 2308 (1994)
34. J. Libuda et al., Surf. Sci. **318**, 61 (1994)
35. A. Sandell et al., J. Electron Spectrosc. Relat. Phenom. **76**, 301 (1995)
36. G. Ceballos et al., Chem. Phys. Lett. **359**, 41 (2002)
37. S. Ulrich, N. Nilius, H.-J. Freund, Surf. Sci. **601**, 4603 (2007)
38. T. Nishimura, Y. Hoshino, T. Okazawa, Y. Kido, Phys. Rev. B **77**, 073405 (2008)
39. G. Kresse et al., Science **308**, 1440 (2005)
40. T. Bertrams, A. Brodde, H. Neddermeyer, J. Vac. Sci. Technol. B **12**, 2122 (1994)
41. K.F. McCarty, J.P. Pierce, B. Carter, Appl. Phys. Lett. **88**, 141902 (2006)
42. M. Schmid et al., Phys. Rev. Lett. **97**, 046101 (2006)
43. M. Kulawik, N. Nilius, H.-J. Freund, Phys. Rev. Lett. **96**, 036103 (2006)
44. N. Nilius et al., Phys. Rev. Lett. **100**, 096802 (2008)
45. M. Morgenstern et al., Phys. Rev. B **62**, 7257 (2000)

46. B.C. Stipe, M.A. Rezaei, W. Ho, Science **280**, 1732 (1998)
47. A. Hewson, *From the Kondo Effect to Heavy Fermions* (Cambridge University Press, Cambridge, 1993)
48. H.A. Mizes, J.S. Foster, Science **244**, 559 (1989)
49. C.G. Slough et al., Phys. Rev. B **34**, 994 (1986)
50. M. Sterrer et al., J. Phys. Chem. B **110**, 46 (2006)
51. M. Sterrer et al., Phys. Rev. Lett. **98**, 096107 (2007)
52. M. Yulikov et al., Phys. Rev. Lett. **96**, 146804 (2006)
53. G. Pacchioni, L. Giordano, M. Baistrocchi, Phys. Rev. Lett. **94**, 226104 (2005)
54. D. Ricci, A. Bongiorno, G. Pacchioni, U. Landman, Phys. Rev. Lett. **97**, 036106 (2006)
55. M. Radmacher et al., Biophys. J. **66**, 2159 (1994)
56. D.R. Baselt, J.D. Baldeschwieler, J. Appl. Phys. **76**, 33 (1994)
57. D.D. Koleske et al., Rev. Sci. Instrum. **66**, 4566 (1995)
58. S. Morita, Y. Sugawara, K. Yokoyama, T. Uchihashi, Nanotechnology **11**, 120 (2000)
59. A. Schirmeisen, D. Weiner, H. Fuchs, Phys. Rev. Lett. **97**, 136101 (2006)
60. T. Minobe et al., Appl. Surf. Sci. **140**, 298 (1999)
61. H. Hölscher, S.M. Langkat, A. Schwarz, R. Wiesendanger, Appl. Phys. Lett. **81**, 4428 (2002)
62. S.M. Langkat, H. Hölscher, A. Schwarz, R. Wiesendanger, Surf. Sci. **527**, 12 (2003)
63. A.I. Livshits, A.L. Shluger, A.L. Rohl, A.S. Foster, Phys. Rev. B **59**, 2436 (1999)
64. P.V. Sushko, A.L. Shluger, C.R.A. Catlow, Surf. Sci. **450**, 153 (2000)
65. A. Sanchez et al., J. Phys. Chem. A **103**, 9573 (1999)
66. L. Giordano, F. Cinquini, G. Pacchioni, Phys. Rev. B **73**, 045414 (2005)
67. V. Simic-Milosevic et al., J. Am. Chem. Soc. **130**, 7814 (2008)
68. H.-J. Freund, Surf. Sci. **601**, 1438 (2007)
69. J. Goniakowski, C. Noguera, Interface Sci. **12**, 93 (2004)
70. Y.-C. Yeo, T.-J. King, C. Hu, J. Appl. Phys. **92**, 7266 (2002)
71. G. Binnig, H. Rohrer, Surf. Sci. **126**, 236 (1983)
72. K.H. Gundlach, Solid-State Electron. **9**, 949 (1966)
73. G. Binnig, H. Roherer, Helv. Phys. Acta **55**, 726 (1982)
74. O.Y. Kolesnychenko, Y.A. Kolesnichenko, O. Shklyarevskii, H. van Kempen, Physica B **291**, 246 (2000)
75. N.D. Lang, Phys. Rev. B **37**, 10395 (1988)
76. C.J. Chen, *Introduction to Scanning Tunneling Microscopy* (Oxford University Press, New York, 1993)
77. L. Olesen et al., Phys. Rev. Lett. **76**, 1485 (1996)